Draft version August 9, 2013
Preprint typeset using LaTeX style emulateapj v. 04/03/99

HST NICMOS OBSERVATIONS OF FSC10214+4724

A. S. Evans[1,2], N. Z. Scoville[1], N. Dinshaw[3], L. Armus[4], B. T. Soifer[1,4], G. Neugebauer[1], and M. Rieke[5]

Draft version August 9, 2013

ABSTRACT

High-resolution, 1.10, 2.05, 2.12, and 2.15 μm imaging of the gravitationally lensed system FSC10214+4724 are presented. These data extend Hubble Space Telescope (HST) observations of the lens system to redder wavelengths, thus providing the highest resolution images to date of the rest-frame optical and narrow-line (i.e., Hα+[N II]) regions of the background quasar. The length of the arc in the wide-band continuum images increases with increasing wavelength, and the Hα+[N II] emission has a length in between that of the 1.10 and 2.05 μm. The structure of the arc changes from having an eastern and western peak at 1.10 μm to a single peak in the center at 2.05 μm. The changing structure and length of the arc can be understood in terms of a model where the background quasar consists of a region of scattered AGN light that dominates at 1.10 μm (rest-frame 3300Å), surrounded by a more extended narrow-line region. An even more extended red stellar population would thus contribute light at 2.05 μm (rest-frame 6200Å). In addition, the Hα+[N II] emission has structural features similar to the 1.10 μm emission normalized by the (predominantly stellar) 2.05 μm emission, possibly confirming that the 1.10 μm emission is a superposition of the sources associated with the line emission (AGN/massive stars) and the red stellar component that dominates the 2.05 μm emission.

The counterimage of the lensed quasar is detected in the 1.10 and 2.05 μm images, and the rest-frame 3300 and 6200Å magnifications of the lensed quasar are calculated to be 50±11 and 25±6, respectively, which translates into rest-frame optical luminosity for the quasar of $\sim 6 \times 10^9$ L$_\odot$. These magnification values are lower than the previously measured magnification of ~ 100 at rest-frame 2400Å. If the dust in the primary lensing galaxy is not affecting the measurement of the counterimage flux at 2400 and 3300Å, the magnification of the quasar appears to decrease with increasing wavelength.

Flux measurements of the primary lensing galaxy fit the spectral energy distribution of an unevolving elliptical galaxy at a redshift of 0.9, consistent with previous determinations of the redshift.

Subject headings: early universe—galaxies: gravitational lensing—infrared: active—galaxies: individual (IRAS FSC10214+4724)

1. INTRODUCTION

Since its discovery (Rowan-Robinson et al. 1991), the high-redshift, far-infrared selected source FSC10214+4724 has been studied in exhaustive detail. Much of the work done prior to 1994 was inspired by the belief that FSC10214+4724 was in the early stages of formation; large quantities of dust and star-forming molecular gas were inferred from its high observed far-infrared (Rowan-Robinson et al. 1991) and CO luminosities (Brown & Vanden Bout 1992; Solomon, Downes, & Radford 1992). Evidence for a buried active galactic nucleus (AGN) was also deduced from imaging polarimetry (Lawrence et al 1993) and rest-frame optical emission-line diagnostics (Elston et al. 1994; Soifer et al. 1995; Iwamuro et al. 1995), indicating that, in addition to starlight, much of the observed luminosity ($L_{\rm ir}[8-1000\mu{\rm m}] \sim 10^{14}$ L$_\odot$) might be reprocessed AGN light. Growing suspicion that FSC10214+4724 might be gravitationally lensed by foreground galaxies (Elston et al. 1994; Matthews et al. 1994; Trentham 1995) led to a series of observations employing various techniques to achieve the highest possible resolution (e.g., Graham & Liu 1995; Broadhurst & Lehár 1995; Serjeant et al. 1995; Close et al. 1995). However, it was not until FSC10214+4724 was observed with the HST Wide-Field Planetary Camera 2 (WFPC2) that its nature was conclusively resolved; the 0.8 μm (rest-frame 2400Å) image showed unambiguously the lensed quasar, counterimage, and lensing galaxies (Eisenhardt et al. 1996, hereafter E96).

The fact that FSC10214+4724 is a gravitationally lensed system makes it no less intriguing a source. Indeed, lensing has made it possible to study the properties of distant galaxies that would otherwise be too faint to observe. Further, because the likelihood of lensing increases with the increased distance (and thus the increased volume of intervening galaxies) of the background galaxy to the observer, many galaxies found at the highest redshifts may be lensed as well.

The availability of the recently installed Near-Infrared Camera and Multiobject Spectrometer (NICMOS) on HST has made it possible to obtain high resolution ($\sim 0.1'' - 0.2''$) images of the continuum and narrow emission-

[1]Division of Physics, Math, & Astronomy, California Institute of Technology, Pasadena, CA 91125
[2]Email Address: ase@astro.caltech.edu
[3]UCO/Lick Observatory, University of California, Santa Cruz, CA 95064
[4]SIRTF Science Center, California Institute of Technology, Jet Propulsion Laboratory, Pasadena, CA 91125
[5]Steward Observatory, University of Arizona, Tucson, AZ 85721

line regions in the lensed quasar at rest-frame wavelengths redward of 2700Å. Specifically, optical radiation emitted from a source at $z \sim 2.3$ is redshifted to near-infrared wavelengths in the present epoch, and thus a program to image the lensed quasar at rest-frame optical wavelengths and in Hα+[N II] with NICMOS has been carried out. Because of the effects of dust and the possible differences in the size scales of the continuum and line emission regions, the extent and structure of the arc will likely change as a function of wavelength. Of equal importance is the amount to which the intrinsic luminosity of the quasar is amplified as a function of wavelength. This effect is due to the fact that different regions of the background object have different colors, and are thus amplified by different amounts. For FSC10214+4724, the magnification is determined from the fluxes of the arc and counterimage (E96). Finally, these observations provide additional photometric data to complement WFPC2 and ground-based measurements of the lensed quasar and lensing galaxies.

The paper is divided into five sections. The HST observations and data reduction are summarized in §2. A detailed description of arc is provided in §3, along with a brief description of the photometry. In §4, the properties of the lensed quasar and the lensing galaxies are deduced. Section 5 summarizes the paper.

Throughout this paper, $H_0 = 75$ km s^{-1} Mpc^{-1} and a $q_0 = 0.5$ are adopted, such that for a source at a $z = 0.9$, 5.6 kpc subtends $1''$ on the sky. For sources at redshifts of 0.9 and 2.286, the luminosities distances are 4170 and 11780 Mpc, respectively.

2. OBSERVATIONS AND DATA REDUCTION

HST observations of FSC10214+4724 were obtained in a single orbit on 1997 October 27 (UT) using camera 2 of NICMOS. Camera 2 consists of a 256×256 HgCdTe array with pixel scales of $0.0762''$ and $0.0755''$ per pixel in x and y, respectively, providing a $\sim 19.5'' \times 19.3''$ field of view (Thompson et al. 1998). Images were obtained using the wide-band ($\Delta\lambda_{\rm FWHM} \sim 0.6$ μm) F110W (1.10 μm) and F205W (2.05 μm) filters, providing a full width at half the maximum flux (FWHM) for a point source of $0.11''$ and $0.20''$, respectively. Observations were done by executing a 4-point spiral dither per filter setting; the step size used was 25.5 pixels ($1.91''$). At each dither position, non-destructive reads (MULTIACCUM) were obtained, with integration times of 96 seconds per dither position. The total integration time per wide-band filter setting was thus 384 seconds.

Two narrow-band ($\Delta\lambda_{\rm FWHM} \sim 0.02$ μm) images of FSC10214+4724 were also taken. The F215N filter (2.15 μm) is centered at the wavelength of the redshifted Hα+[N II] emission, and the F212N filter (2.12 μm) is centered at 6450Å in the rest-frame of the lensed quasar (i.e., continuum only). The FWHM of a point source in both filters is $\sim 0.21''$. Observations with the narrow-band filters were done in the same fashion as the wide-band filters, with longer integration times of 120 seconds at each dither position. The total integration time per filter setting was thus 480 seconds. Finally, dark exposures were taken using the same MULTIACCUM sequences executed for the quasar observations.

Reduction of the data was done with IRAF. The dark was first created, then the NICMOS data were dark subtracted, flatfielded and corrected for cosmic rays using the IRAF pipeline reduction routine CALNICA (Bushouse 1997). The dithered images were then shifted and averaged using the DRIZZLE routine in IRAF (e.g. Hook & Fruchter 1997). The plate scales of the final "drizzled" images are $0.0381''$ and $0.0378''$ per pixel in x and y, respectively. The resultant images are shown in Figure 1.

Of key interest to this project is the relative positioning of the arc and the counterimage to the lensing galaxies as a function of wavelength. To check the accuracy of the pointing during the observations, the relative positions of Source 2 (see §3.1) were measured in the wide-band images using the IRAF routine IMEXAMINE; the centroid of Source 2 in the two images differed by only 0.04 ($0.0015''$) of a pixel.

Finally, flux calibration of the images were done using the scaling factors 2.28×10^{-6}, 1.55×10^{-6}, 4.07×10^{-5}, and 4.48×10^{-5} Jy (ADU/sec)$^{-1}$ at 1.10, 2.05, 2.12, and 2.15 μm, respectively (Rieke et al. 1998). The corresponding magnitudes were calculated using the zero-points 1909, 707, 686 and 680 Jy (Rieke et al. 1998).

3. RESULTS

For ease in direct comparison, the sources within the field of view (Figure 1) have been numbered in the same manner as done by Matthews et al. (1994) and E96.[6] All of the sources previously observed by E96 were detected in the 1.10 and 2.05 μm images. Source 1 is observed to be an arc with a FWHM of $\sim 0.6''$ in length and unresolved in width. A more detailed description of the arc will be provided in §3.1. The primary lensing galaxy (Source 2) has a compact nuclear region and an underlying, low surface brightness envelope; the FWHM of Source 2 is $\sim 0.29''$ in the 2.05 μm image. Two additional galaxies are visible; the secondary lensing galaxy (Source 3: see E96) is an asymmetric galaxy with a FWHM of $\sim 0.35''$ in the 2.05 μm image and an unresolved nucleus at its western end. Source 4, which is a relatively faint, compact (FWHM $\lesssim 0.20''$) galaxy in the 2.05 μm image, appears to be a highly inclined galaxy in the WFPC2 image (E96). Source 5, the counterimage of the lensed quasar, appears as a faint northern extension of Source 2, and will be discussed in more detail in §4.1.

3.1. *Arc Structure*

Figure 2 consists of a contour plot of the 0.8 μm image of Sources 1 and 2 taken from E96, and contour plots of the 1.10, 2.05, and 2.15 μm images. The tangential extent of the arc differs in the wide-band images; the full width at 10% the maximum flux density of Source 1 subtends an angle of $\sim 46^{\rm o}$ at 0.8 μm relative to the position of the primary lensing galaxy (Source 2), $\sim 46^{\rm o}$ at 1.10 μm, and $\sim 71^{\rm o}$ at 2.05 μm. Given that Source 2 is $\sim 1.2''$ north of Source 1 (as measured from the peak of Source 1 at 2.05 μm), the arc has observed lengths of $\sim 0.95''$, $0.95''$, and $1.5''$ at 0.8, 1.10, and 2.05 μm, respectively.

Using the same criteria as above, the narrow-band, 2.15

[6]References to Sources 1-4 should be made in accordance with the *IAU* naming convention FSC 10214+4724:M (number). Likewise, Source 5 should be referred to as FSC10214+4724:E 5.

μm image of the arc subtends an angle of $\sim 61^{\rm o}$ relative to the primary lensing galaxy, and is thus $1.3''$ in length. As expected, the arc is unresolved in width at 2.15 μm. In the 2.12 μm continuum image, the arc is relatively faint, indicating that continuum emission comprises only a small fraction of the 2.15 μm flux. Further, aside from the lensed quasar, there appear to be no strong ($m_{2.15} < 18.3$ mag) emission-line sources at the redshift of Source 1 present in the field.

Figure 3 shows close-up, contour plots of Source 1. As noted by E96, the 0.8 μm image of Source 1 is asymmetric, having a primary eastern peak separated from a secondary western peak by $\sim 0.24''$ (Figure 3a). The 1.10 μm (i.e., rest-frame 3300Å) emission from the arc has an asymmetric appearance similar to the 0.8 μm (rest-frame 2400Å) emission; the arc has an asymmetric appearance, with a major peak (P1) on the eastern end of the arc separated by $\sim 0.27''$ from a faint, minor peak (P2) on the western end. In contrast to the 0.8 and 1.10 μm emission, the 2.05 μm (rest-frame 6200Å) emission has a nearly symmetric appearance, with a single peak at the center of the arc. The position of the primary 1.10 μm and the 2.05 μm peaks differ by $0.10''$.

Figure 3f shows the ratio of the 1.10 and 2.05 μm images. The image consists of a two-component arc with fainter emission bridging the components. The primary peak of the image is marginally shifted ($0.04''$) eastward of the primary 1.10 μm peak (P1), and the secondary peak is shifted a similar amount from the secondary 1.10 μm peak (P2).

Figure 3g and 3h show the contour plots of the 2.15 μm image and the difference of the 2.15 and 2.12 μm images (i.e., Hα+[N II]). Because the peak of the 2.12 μm image appears shifted $\sim 0.10''$ west of the 2.05 μm peak, an additional check of the structure of the Hα+[N II] emission was done by scaling the 2.05 μm image to the flux of the 2.12 μm image, then subtracting it from the 2.15 μm image; the resultant arc showed only marginal changes from the subtraction using the 2.12 μm image. The similarities between the images shown in Figure 2g and 2h are due to the large contribution of line emission to the overall flux density and structure of the 2.15 μm emission.

3.2. *Photometry*

Table 1 lists the magnitudes derived from the images in Figure 1, as well as magnitudes in the wavelength range 0.7–2.2 μm compiled from the literature. The magnitudes for all of the sources are consistent with previous ground-based measurements. Both of the wide-band NICMOS images of Source 1 are composed of continuum and line emission; strong Ne V and Ne III emission have been detected in the wavelength range 1.1–1.3 μm (Soifer et al. 1995; Iwamuro et al. 1995), and Hα+[N II] emission has been observed at 2.15 μm (Elston et al. 1994; Soifer et al. 1995). The percentage of line contribution to the 2.05 μm flux of Source 1 can be calculated from the narrow-band images. Subtracting the 2.12 μm continuum image from the 2.15 μm and measuring the flux of the resultant emission-line image, the Hα+[N II] flux is calculated to be $4.3(\pm 0.4) \times 10^{-18}$ W m^{-2}, 30–50% lower than the values of 6×10^{-18} W m^{-2} and 7×10^{-18} W m^{-2} determined by Matthews et al. (1994) and Elston et al. (1994), respectively. Thus, Hα+[N II] comprises $\sim$12% of the 2.05 μm flux of Source 1. This percentage is consistent with the approximate value of 13% calculated from the near-infrared spectrum of FSC10214+4724 by Soifer et al. (1995). Similarly, using the Hα+[N II] flux in combination with the Ne V and Ne III to Hα+[N II] flux ratio of 1.1 determined by Soifer et al. (1995), the Neon emission lines are calculated to comprise $\sim$8% of the 1.10 μm flux.

4. DISCUSSION

Both the length and structure of the continuum and line emission of Source 1 can be explained in terms of the relative sizes of the emission regions, the structure of the emission regions, and their location near the cusp of a caustic (i.e., line of infinite magnification: see Blandford & Narayan 1992). Given that Source 1 is a dust enshrouded quasar (§1), it is very likely that a substantial fraction of the luminosity from Source 1, especially at bluer wavelengths, is scattered/reprocessed AGN light. The length of the wide-band continuum emission has been shown to increase as a function of wavelength (§3.1), indicating that the light emitted at longer wavelengths is closer to the caustic than the shorter wavelength light. Physically, this can be understood if the 0.8–1.10 μm light emanates predominantly from regions of scattered AGN light, and the 2.05 μm light emanates from the underlying, red stellar population of Source 1 which is more extended than the scattered light region and has a substantial cross-section on or near the caustic. By comparison, the Hα+[N II] emission, which traces light from the narrow-line regions (e.g. Osterbrock 1989), has a length in between that of the 0.8–1.10 μm and 2.05 μm emission, indicating that the narrow-line region is more extended than the scattered AGN light region, but not as extended as the stellar region traced by the 2.05 μm emission.

The change in the structure along the arc is indicative of variations in the morphology of Source 1 as a function of wavelength. While the 0.8 and 1.10 μm emission have an eastern and western peak, the fact that the 2.05 μm emission has only one peak at the center of the arc may be a result of the red stellar emission being more extended than or displaced relative to the 0.8–1.10 μm emission. Further, the two-component morphology of the emission-lines is similar to the ratio of the 1.10 and 2.05 μm emission. Normalizing the 1.10 μm emission by the 2.05 μm emission removes structure at 1.10 μm caused by the red stellar population. Thus, the similarities between the structure of the line emission and the 1.10 μm / 2.05 μm ratio may confirm that the 1.10 μm emission is a superposition of a blue component associated with the emission-line emission and a red stellar component that dominates at 2.05 μm. Such superpositions have also been modeled in radio galaxies at $z \sim 1$, where the images of the galaxies at bluer wavelength appear to be comprised of an elongated component, as well as a symmetric component similar in shape to the symmetric images of the galaxies at redder wavelengths (Rigler et al. 1992).

4.1. *Magnification*

Figure 4 shows 0.8, 1.10, and 2.05 μm contour plots of Source 2 and the counterimage (Source 5). There appears to be a marginal shift in the centroid of Source 5 at 2.05 μm relative to 0.8 and 1.10 μm; such a shift may simply

be an artifact of low signal-to-noise, or it may be further evidence that the morphology of the 0.8–1.10 and 2.05 μm emission from the quasar are different, thus causing the counterimage to appear at a slightly different location on the image plane.

In order to determine the 1.10 and 2.05 μm fluxes of the counterimage, which is necessary for determining the magnification of the quasar, the flux in a 0.38″ diameter aperture centered on the counterimage was measured, then fluxes were measured in seven apertures positioned the same distance from the center of Source 2 as the counterimage aperture. The rms of the eight positions was then used to determine the rms of the measured flux of Source 5. The flux densities were determined to be 0.76±0.11 and 3.3±0.78 μJy at 1.10 and 2.05 μm, respectively. The total magnification of FSC10214+4724 is simply the ratio of the arc to counterimage flux densities (E96), thus the magnification of the lensed quasar is 50±11 and 25±6 at rest-frame 3300 and 6200Å, respectively. If the assumption is made that the emission emanates from a uniformly illuminated source (Figure 5 of E96), the source of the emission is ∼100 pc (0.015″) in radius at 3300Å, and ∼300 pc (0.04″) in radius at 6200Å. Further, correcting the observed luminosities of the quasar for the lensing factors yields rest-frame 3300 and 6200Å luminosities of $2.8(\pm0.6)\times10^9$ and $6.3(\pm1.7)\times10^9$ $L_\odot$. Typical rest-frame optical luminosities of ultraluminous infrared galaxies are $\sim 1\times10^{10}$ $L_\odot$, but variations in their rest-frame optical luminosities result, in part, from dust obscuration.

The magnification of the lensed quasar has previously been determined at wavelength blueward of rest-frame 3000Å. E96 calculated a rest-frame 2400Å magnification of ∼ 100, and Nguyen et al. (1998) has computed a lower limit of the rest-frame 1300Å magnification of ∼ 250. Thus, the magnification of the lensed quasar appears to be decreasing with increasing wavelength. However, as Nguyen et al. (1998) point out, while the arc is most likely too far from the primary lensing galaxy (Source 2) for its measured flux to be diminished by dust in the lensing galaxy, the proximity of the counterimage to the nucleus of the Source 2 may mean that the flux of the 1300-3300Å counterimage, and thus the flux ratio of the arc to counterimage at 1300-3300Å, are heavily affected by dust in the primary lensing galaxy. By the same argument, the radiation from the lensed quasar which is detected in the 2.05 μm filter has a wavelength of 1.1 μm as it passes near the primary lensing galaxy, and thus is unaffected by dust.

4.2. *The Redshift of the Lensing Galaxies*

As mentioned in §3.2, the measured fluxes of all of the sources agree with previous ground-based measurements. Of particular interest is the redshift and Hubble type of the lensing galaxies as derived from their fluxes and the morphologies. The NICMOS data presented here are consistent with the assertion that Source 2 is an early-type galaxy at a redshift of 0.9 (see discussion of the spectral energy distribution of Source 2 in Appendix A of E96). While such a straightforward interpretation of the spectral energy distribution (SED) of Source 3 is not possible, the close proximity of the two galaxies and the similarity in their observed extent indicate that Source 3 is very likely a companion of Source 2. If both galaxies are at the same redshift, they have a projected separation of ∼ 14 kpc and size scales (FWHM) of ∼ 1.8 kpc, and it is very likely that the asymmetric appearance of Source 3 results from a tidally interaction with Source 2. The optical luminosities of Source 2 and 3, as derived from the observed 1.10 μm magnitudes, are 4.5×10^9 and 2.3×10^9 $L_\odot$, respectively, which is comparable to the luminosities of the bulges of local spiral galaxies (M31 and the Milky Way galaxies) and of low luminosity elliptical galaxies, but an order of magnitude lower than the average luminosity of present day elliptical galaxies (i.e., Nieto et al. 1990).

5. SUMMARY

High-resolution near-infrared imaging of the lens system FSC10214+4724 has been presented. The observations have provided the highest resolution images to date of the rest-frame optical and narrow-line region emission from the lensed quasar. The following conclusions are reached:
(1) The length of the wide-band continuum emission (Source 1) increases with increasing wavelength. The full width at 10% the maximum flux level of Source 1 is 0.95″ in length at 1.10 μm and 1.5″ in length at 2.05 μm. In comparison, the length of the 0.8 μm arc (E96) is also 0.95″. Thus, if the 0.8–1.10 μm emission occurs mostly from a region of scattered AGN light, the 2.05 μm emission may be dominated by red stellar light from a more extended region having a cross-section that overlaps or is near the caustic.
(2) The 1.10 μm image of the arc has a primary eastern and secondary western peak, similar to the 0.8 μm emission. In contrast, the 2.05 μm emission is symmetric, having a peak at the center of the arc. This indicates that the red stellar emission is displaced from the emission from scattered AGN light.
(3) The Hα+[N II] emission has a length in between that of the 1.1 and 2.05 μm emission. This may indicate that the narrow-line region is more extended than the scattered AGN light region, but not as extended as the red stellar distribution. Further, the Hα+[N II] emission-line image of the arc appears to have a structure similar to the 1.10 μm emission normalized by the (predominantly stellar) 2.05 μm emission, consistent with the idea that the 1.10 μm emission is a superposition of sources associated with the emission lines and the stellar component that dominates the 2.05 μm emission.
(4) The Hα+[N II] emission in Source 1 has an observed flux of $4.3(\pm0.4)\times10^{-18}$ W m^{-2}. This line emission is calculated to comprise 12% of the wide-band 2.05 μm flux of the lensed quasar. An 8% level of emission-line contamination is deduced for the 1.10 μm flux.
(5) The rest-frame 3300 and 6200Å magnifications of the lensed quasar are estimated to be 50±11 and 25±6, respectively. Thus, the quasar is determined to have a rest-frame optical luminosity of $\sim 6\times10^9$ $L_\odot$.
(6) The measured flux densities of the primary lensing galaxy (Source 2) are consistent with previous near-infrared measurements and support the idea that it is an early-type galaxy at a redshift of 0.9.

ASE thanks C. Fassnacht, J. Carpenter, J. Surace, and B. Stobie for useful discussion and assistance. We also thank the referee for many useful comments. This research was supported by NASA grant NAG 5-3042, and

the observations were obtained with the NASA/ESA Hubble Space Telescope operated by the Space Telescope Science Institute managed by the Association of Universities for Research in Astronomy Inc. under NASA contract NAS5-26555.

REFERENCES

Blandford, R. D. & Narayan, R. 1992, ARAA, 30, 311
Broadhurst, T. & Lehár, J. 1995, ApJ, 450, L41
Brown, R. L., & Vanden Bout, P. A. 1992, ApJ, 397, L19
Bushouse, H. 1997, in HST Calibration Workshop, eds. S. Casertano, R. Jedrzejewski, T. Keyes, & M. Stevens (Baltimore), 223
Close, L. M., Hall, P. B., Liu, C. T., & Hege, E. K. 1995, ApJ, 452, L9
Eisenhardt, P. R., Armus, L., Hogg, D. W., Soifer, B. T., Neugebauer, G., & Werner, M. W. 1996, ApJ, 461, 72 (E96)
Elston, R., McCarthy, P. J., Eisenhardt, P., Dickinson, M., Spinrad, H., Januzzi, B. T., & Mahoney, P. 1994, AJ, 107, 910
Graham, J. R. & Liu, M. C. 1995, ApJ, 449, L29
Hook, R. N. & Fruchter, A. S. 1997, Astronomical Data Annalysis, Software & Systems VI, A.S.P. Conference Series, eds. G. Hunt & E. Payne, 125, 147
Iwamuro, F., Maihara, T., Tsukamoto, H., Oya, S., Hall, D. N. B., & Cowie, L. L. 1995, PASJ, 47, 265
Lawrence, A. et al. 1993, MNRAS, 260, 28
Matthews, K. et al. 1994, ApJ, 420, L13
Nieto, J.-L., Bender, R., Davoust, E., & Prugniel, P. 1990, A&A, 230, L17
Nguyen, H. T., Eisenhardt, P. R., Werner, M. W., Goodrich, R., Hogg, D. W., Armus, L., Soifer, B. T., Neugebauer, G. 1998, AJ, in press
Osterbrock, D. E. 1989, Astrophysics of Gaseous Nebulae and Active Galactic Nuclei (California: University Science Books)
Rieke, M. et al. 1998, in preparation
Rigler, M. A., Lilly, S. J., Stockton, A., Hammer, F., & Le Fèvre, O. 1992, ApJ, 385, 61
Rowan-Robinson, M., et al. 1993, MNRAS, 261, 513
Serjeant, S., Lacy, M., Rawlings, S., King, L. J., & Clements, D. L. 1995, MNRAS, 276, L31
Soifer, B. T., Cohen, J. G., Armus, L., Matthews, K., Neugebauer, G., & Oke, J. B. 1995, ApJ, 443, L65
Solomon, P. M., Downes, D., & Radford, S. J. E. 1992a, ApJ, 398, L29
Thompson, R. I., Rieke, M., Schneider, G., Hines, D. C., & Corbin, M. R. 1998, ApJ, 492, L95
Trentham, N. 1995, MNRAS, 277, 616

TABLE 1
MAGNITUDES FOR SOURCES IN FSC10214+4724 FIELD

Source	$m_{0.70}$[a]	$m_{0.79}$[b]	$m_{1.10}$[c]	$m_{1.25}$[d]	$m_{1.6}$[d]	$m_{2.05}$[c]	$m_{2.17}$[d]	$m_{2.12}$[c]	$m_{2.15}$[c]
1	20.72±0.02[e]	20.44[f]	19.2±0.1[g]	19.0[g]	16.9±0.02	17.3±0.1[h]	17.4[h]	17.2±0.2	15.4±0.1[h]
2	22.93±0.12	20.3	20.1±0.1	19.4	18.51±0.06	18.0±0.1	17.6	···	···
3	23.13±0.25	22.98	21.6±0.2[e]	20.7	19.52±0.16	18.9±0.1	18.5	···	···
4	···	23.58	22.6±0.2[e,i]	22.4	···	20.0±0.1[i]	20.0	···	···
5	···	25.5	23.5±0.2[j]	···	···	20.8±0.2[j]	···	···	···

[a]From Elston et al. (1994).

[b]From Eisenhardt et al. (1996).

[c]This paper. Unless otherwise noted, all 1.10, 2.05, 2.12, and 2.15μm magnitudes have been calculated using a 1.37″ diameter aperture.

[d]From Matthews et al. (1994).

[e]Contains emission from CIII] λ1909 and Ne IV] λ2424 lines.

[f]Contains emission from Ne IV] λ2424 lines.

[g]Contains emission from [Ne V] $\lambda\lambda$ 3346,3426 and [Ne III] $\lambda\lambda$ 3869,3967 lines.

[h]Contains emission from Hα+[N II] $\lambda\lambda$6548,6583 lines.

[i]Calculated using a 0.68″-diameter aperture.

[j]Calculated using a 0.38″-diameter aperture.

Figure Captions

Figure 1a–d: NICMOS 1.10, 2.05, 2.12, and 2.15 μm images of the field of FSC10214+4724. The arc (Source 1) is unresolved in width in all the images. Note that the noise in the top left-hand corner of each image is due to the coronagraphic hole on camera 2 of NICMOS.

Figure 2. Contours of Sources 1 and 2. (a) The wide-band 0.8 μm image taken from E96. The peak flux density is 0.22 μJy. (b,c) The wide-band 1.10 and 2.05 μm images, with peak flux densities of 0.27 and 0.5 μJy. (d) The narrow-band image, with a peak flux density of 2.4 μJy. All contours are displayed at 10, 21, 32, 43, 54, 66, 77, 88, and 99% of the peak image flux.

Figure 3. (a,b) Wide-band 0.8 and 1.10 μm contours of Source 1, with peak fluxes densities of 0.37 and 0.48 μJy. (c-h) Contours of Source 1 smoothed to a resolution of $\sim 0.23''$. (c,d,e) The wide-band 0.8, 1.10 μm and 2.05 μm images, with peak flux densities of 0.22, 0.27 and 0.50 μJy. (f) The ratio of the 1.10 and 2.05 μm images, with peak flux density ratio of 0.52. (g) The narrow-band 2.15 μm image, with a peak flux density of 2.4 μJy. (h) The continuum-subtracted Hα+[N II] image, with a peak flux density of 2.1 μJy. All contours are displayed at 60, 65, 70, 75, 80, 84, 89, 94, and 99% of the peak image flux.

Figure 4. Contour plots of Sources 1, 2, and 5 at 0.8, 1.10, and 2.05 μm. The images have been gaussian smoothed to a resolution of $0.23''$, then boxcar smoothed 3×3 (0.8 μm image) and 4×4 (1.10 and 2.05 μm images) pixels. The contour levels in each image have been chosen to highlight Source 5, and thus correspond to nine linearly spaced contour levels over the flux densities ranges 0.0090–0.014, 0.011–0.020, and 0.038–0.085 μJy for 0.8, 1.10, and 2.05 μm , respectively.

This figure "asefig1.jpg" is available in "jpg" format from:

http://arxiv.org/ps/astro-ph/9812196v1

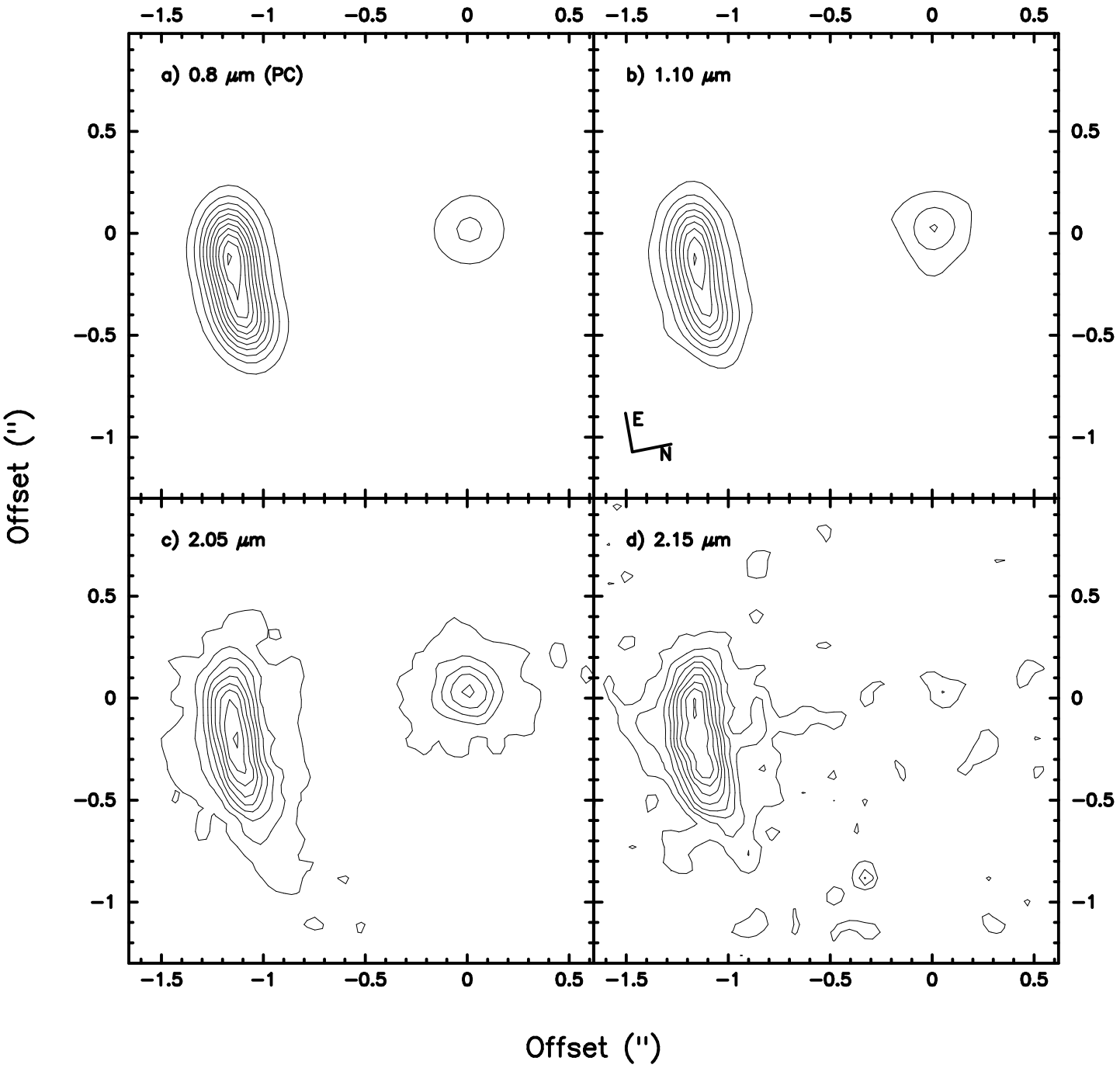
a) 0.8 μm (PC)
b) 1.10 μm
c) 2.05 μm
d) 2.15 μm
E
N
−1.5
−1
−0.5
0
0.5
Offset (")
Offset (")

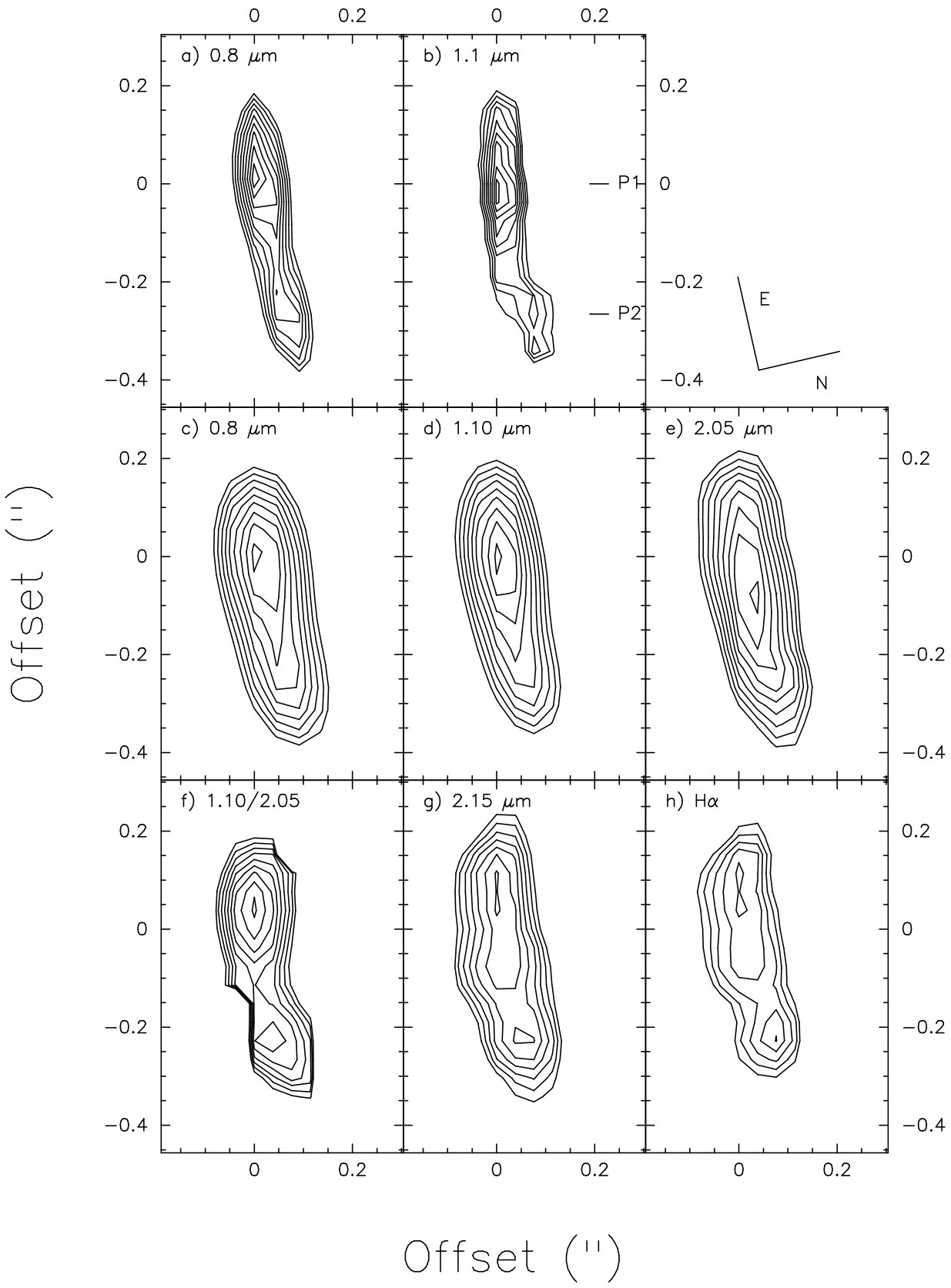
a) 0.8 μm
b) 1.1 μm
c) 0.8 μm
d) 1.10 μm
e) 2.05 μm
f) 1.10/2.05
g) 2.15 μm
h) Hα
P1
P2
E
N
0
0.2
−0.2
−0.4
Offset (")
Offset (")

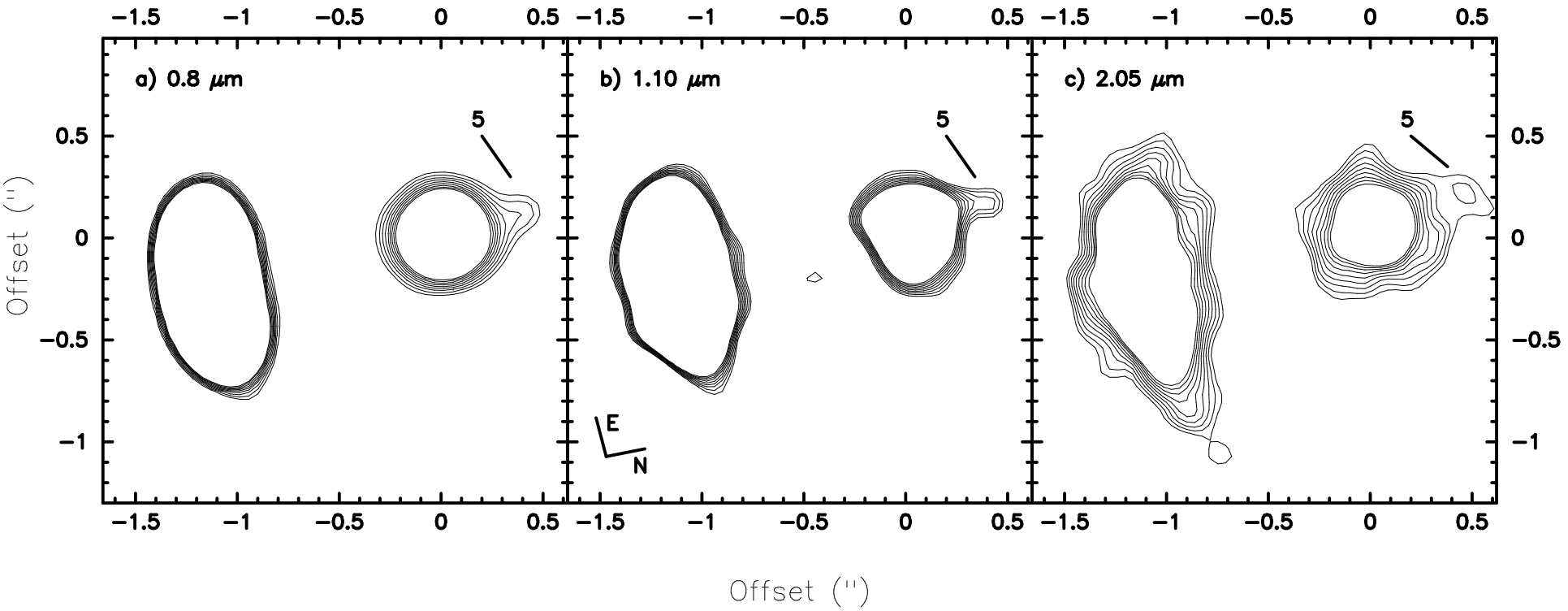
a) 0.8 μm
b) 1.10 μm
c) 2.05 μm
5
5
5
E
N
−1.5
−1
−0.5
0
0.5
Offset (")
Offset (")